A&A 421, 1031–1043 (2004)
DOI: 10.1051/0004-6361:20034156

Astronomy & Astrophysics

Synoptic study of the SMC SNRs using *XMM-Newton*

K. J. van der Heyden[1,2], J. A. M. Bleeker[1], and J. S. Kaastra[1]

[1] SRON National Institute for Space Research, Sorbonnelaan 2, 3584 CA Utrecht, The Netherlands
[2] South African Astronomical Observatory, PO Box 9, Observatory 7935, Cape Town, South Africa

Received 4 August 2003 / Accepted 11 March 2004

Abstract. We present a detailed X-ray spectral analysis of 13 supernova remnants (SNR) in the Small Magellanic Cloud (SMC). We apply both single-temperature non-equilibrium ionisation models and models based on the Sedov similarity solution, where applicable. We also present detailed X-ray images of individual SNRs, which reveal a range of different morphological features. Eight remnants, DEM S 32, IKT 2, HFPK 419, IKT 6, IKT 16, IKT 18 and IKT 23, are consistent with being in their Sedov evolutionary phase. IKT 6 and IKT 23 both have a clear shell like morphology with oxygen-rich X-ray emitting material in the centre. We draw attention to similarities between these two remnants and the well studied, oxygen-rich remnant IKT 22 (SNR 0102-72.3) and propose that they are more evolved versions of IKT 22. IKT 5, DEM S 128 and IKT 25 are evolved remnants which are in, or in the process of entering, the radiative cooling stage. The X-ray emission from these three remnants is possibly from the ejecta remains of type Ia SNe. Our modeling allows us to derive estimates for physical parameters, such as densities, ages, masses and initial explosion energies. Our results indicate that the average SMC hydrogen density is a factor of ∼6 lower as compared to the Large Magellanic Cloud. This has obvious implications for the evolution and luminosities of the SMC SNRs. We also estimate the average SMC gas phase abundances for the elements O, Ne, Mg, Si and Fe.

Key words. shock waves – ISM: supernova remnants – X-rays: ISM – galaxies: Magellanic Clouds

1. Introduction

The low interstellar absorption and relative closeness of the Large and Small Magelanic Clouds (LMC and SMC) allows for the study of individual X-ray sources in these galaxies. For supernova remnants (SNRs) in particular, the low absorption makes it possible to detect X-rays in the important 0.5–3.0 keV energy band, which includes emission lines from highly ionised elements such as O, Ne, Mg, Si, S and Fe. The well known distance to the SMC, i.e. 60 kpc (Westerland 1990), allows for good estimates of quantities such as physical size, mass, age and so on.

While the LMC SNRs have been relatively well studied, the remnants in the SMC have not received much attention. For example, Hughes et al. (1998) conducted a systematic study of ASCA-SIS spectra of 7 SNRs in the LMC, while Nishiuchi (2001) analysed 9 fainter remnants. They were able to derive good estimates for the physical parameters of individual SNRs. In contrast, while individual or small samples of SNRs in the SMC have been studied (e.g. Mathewson et al. 1983, 1984; Yokogawa et al. 2002; Hughes & Smith 1994; Nazé et al. 2002), a detailed synoptic X-ray spectral study has not been carried out. This is mainly because SNRs in the SMC are fainter than their LMC counterparts.

To date a total of 16 SNRs have been identified from a number of extensive X-ray surveys with the instruments aboard the *Einstein*, *ASCA* and *ROSAT* Observatories (e.g., Inoue et al. 1983; Wang & Wu 1992; Haberl et al. 2000). The availability of the *Chandra* and *XMM-Newton* Observatories now provides an opportunity to study these remnants with far greater sensitivity and spatial/spectral resolution than before.

We present *XMM-Newton* observations of 13 SNRs in the SMC. Three remnants, viz. SNR 0039-73.9 (Filipovic et al. 1998), SNR 0050-72.8 and SNR 0058-71.8 (last two both Mathewson et al. 1984), have not yet been covered by the *XMM-Newton* SMC observation fields and are thus not included in this paper. The major emphasis of this work is on the spectral analysis of the CCD-resolution data obtained with the European Photon Imaging Cameras (EPIC) (Turner et al. 2001; Strüder et al. 2001). In addition, we also present high resolution spectra of IKT 22 and IKT 23 as measured by the Reflection Grating Spectrometers (RGS) (den Herder et al. 2001).

2. Observations and reduction

Our data are extracted from five pointings towards the SMC. The log of the observations are given in Table 1. The pointings, as listed in Table 1, are centred on the remnants IKT 5, IKT 18, IKT 23 and IKT 22 respectively.

Send offprint requests to: K. J. van der Heyden,
e-mail: heyden@saao.ac.za

The raw EPIC data were initially processed with the *XMM-Newton* Science Analysis System (SAS) version 5.4. This involved the subtraction of hot, dead, or flickering pixels, and the removal of events due to electronic noise. The spectra were extracted using the SAS task *evselect*. We used the standard redistribution matrices available on the VILSPA site, while the ancillary matrices were created using the SAS task *arfgen*. Background subtraction was done by selecting blank sky regions within the same observation.

Mosaic images of the SMC fields were created using our own image and mosaicing software. The image extraction programme selects the photons with the appropriate grades and quality flags and saves the images in FITS file format. The latter is necessary in order to use the standard SAS *eexpmap* programme to make exposure maps for each extracted image. *eexpmap* produces exposure maps normalized to the on axis exposure time, so each exposure map was multiplied with the appropriate EPIC-pn or EPIC-MOS effective area by the mosaicing programme. The routines were called from a script that applied those programmes to each event-list and each channel range.

We also have high resolution spectra of IKT 22 and IKT 23 in addition to the CCD-resolution spectra. RGS spectra of IKT 22 and IKT 23 were obtained with effective exposure times of 70 and 37 ks respectively. The RGS data were processed with SAS version 5.4.

3. Analysis and results

3.1. Images

In Fig. 1 we present a mosaic of our observations. The left image is a mosaic of *XMM-Newton* revolutions 157, 247 and 433, while the right image shows the southwestern part of the SMC (Rev 156). We are able to identify 13 SNRs in our field, these are indicated in Fig. 1 and listed in Table 1. All the remnants are quite soft X-ray sources, with the peak of their emission in the 0.5–1.0 keV band. A number of point sources, which generally display much harder spectra than the remnants, are also visible in the field-of-view. We present detailed colour coded maps of each remnant in Fig. 2. It is clear from Fig. 2 that the remnants exhibit a range of different morphological features. The physical intepretation of these morphologies will be discussed in more detail in Sect. 4.1.

3.2. Spectral analysis

The spectral analysis was performed using the SRON SPEX package (Kaastra et al. 1996), which contains the MEKAL atomic database (Mewe et al. 1995) for thermal emission. Also contained in SPEX are a number of plasma models appropriate for SNR analysis.

We extracted spectra from the entire region of each SNR, while the background spectra were taken from nearby blank-sky regions. The extraction regions were constructed so as to exclude possible point source contamination, where applicable. Broad band EPIC-pn count rates are given are given in Table 2. The estimated percentage point source or possible residual point source contamination (due to the *XMM-Newton* PSF) is also listed in Table 2. The point source fluxes were estimated from the *ROSAT HRI* values. The *XMM-Newton* fluxes were compatible with the *ROSAT HRI* ones. The spectra of individual remnants are shown in Figs. 3 and 4. A typical background spectrum is also displayed in Fig. 4. All our SNR spectra are thermal in nature and show emission from highly ionised atoms of O, Ne, Mg, Si and Fe.

We first attempted to fit all the spectra with a single temperature non-equilibrium ionisation (NEI) model. This assumes that the plasma has been instantly shock-heated to a temperature T_e some time (t) ago. The NEI model does not contain any dynamical model for SNR evolution. In this model we fit the volume emission measure ($n_{es}n_{Hs}V$), the electron temperature (kT_e), the ionisation parameter ($n_{es}t$), the elemental abundances and the column density N_H of absorbing gas along the line of sight. n_{es} and n_{Hs} are the electron and hydrogen density of the shocked gas, respectively and V is the volume of emitting gas. Both IKT 21 and IKT 25 have point sources in the field which could not be unambiguously excluded in the spectrum extraction. Here we have added power-law components to account for the point emission.

During the fitting procedure we initially kept the abundances fixed at the mean SMC ISM value of 0.2 solar (Russel & Dopita 1992). We started by allowing only the normalisations of the plasma components to vary and subsequently we also allowed the temperature, ionisation age, absorption and abundances (where necessary) to vary. The spectra from EPIC-pn and EPIC-MOS were fitted simultaneously, but sparately. The results of the fits are given in Table 3. The abundances are all relative to their solar values (Anders & Grevese 1989). We give the unabsorbed luminosities in the 0.5–2.0 keV band.

We also estimated the electron density and radiating mass based on the best-fit emission measure. Here it is provisionally assumed that the emitting gas is confined to shells of a typical thickness R/12. The radii were estimated from the X-ray images. The mass estimates indicate that most of the sources are evolved remnants that have swept-up a considerable amount of mass and should thus be emitting in their Sedov phases. Moreover, a number of remnants could not be adequately described by the simple NEI model, in particular, the spectra with higher statistics (viz., IKT 6, IKT 22, IKT 23). These spectra appear to show an ionisation and/or temperature distribution. We thus consider a Sedov model to be the most appropriate for fitting the data. This model is based on the Sedov solution (Sedov 1959) which describes the self-similar expansion of an adiabatic blast wave in a homogeneous medium.

We proceed to fit the IKT 6, IKT 18, IKT 22 and IKT 23 spectra with a Sedov model, based on unacceptable χ^2's and large swept-up mass, obtained from the NEI model fits. IKT 6 and IKT 23 have a shell and centrally filled morphology. We extract and fit only the shell part of the spectra of these two remnants with a Sedov model. The *Chandra* data reveal that IKT 22 has a blastwave and reverse shock structure (Hughes et al. 2000), however, *XMM-Newton* cannot resolve these two regions so we fit the spectrum extracted from the entire remnant. Even though IKT 22 is clearly less evolved than IKT 6 and IKT 23 (for example), we do find that the Sedov model

Table 1. *XMM-Newton* EPIC observation log. The abbreviations used are: EF – Extended Full Frame , FF – Full Frame , LW – Large Window, T – Thin Filter, M – Medium Filter.

Rev No.	Obs. ID	Mode		Filt.	Exp. (ks)		RA	Dec
		pn	MOS		pn	MOS	(J2000)	(J2000)
156	0110000101	EF	FF	M	23	27	00 49 07	−73 14 06
157	0110000201	EF	FF	M	16	20	00 59 26	−72 10 11
157	0110000301	EF	FF	M	31	35	01 04 52	−72 23 10
247	0135720601	FF	LW	T	16	33	01 03 50	−72 01 55
433	0135720901	FF	LW	T	14	13	01 04 01	−72 01 51

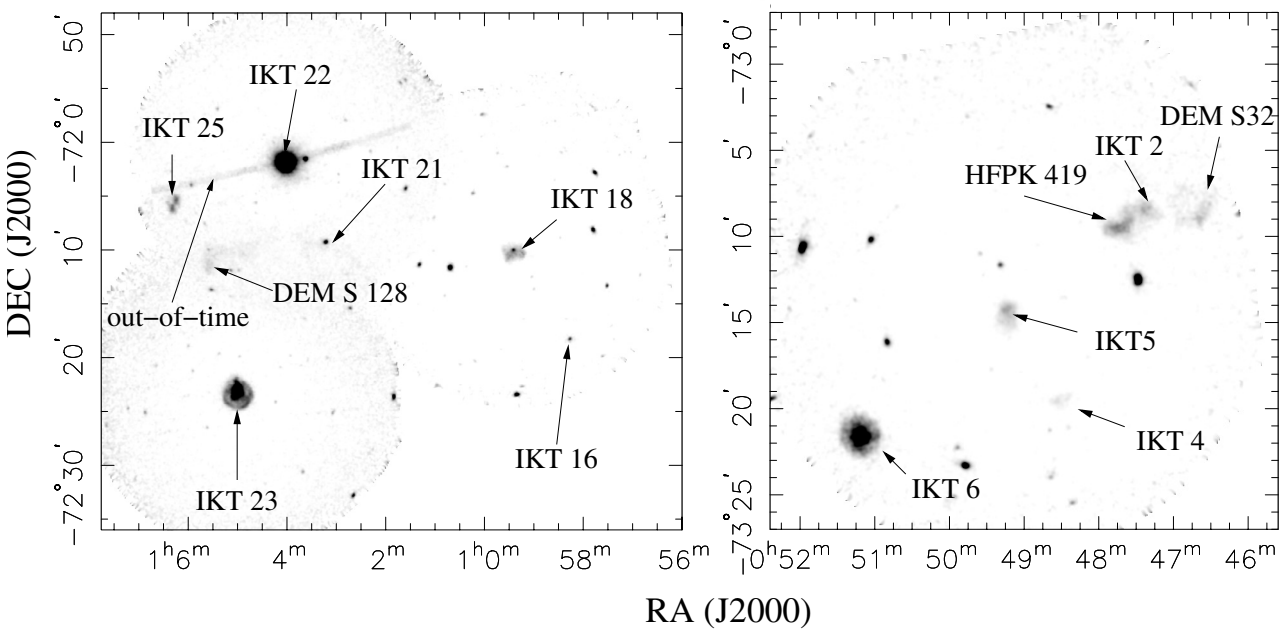

Fig. 1. Mosaic images of the SMC region in the 0.5–3.0 keV energy band. The left image is the combined observations of *XMM-Newton* Rev's 157, 247 and 433, while the right panel is an image of Rev 156. Individual remnants are indicated. The out-of-time events from IKT 22 can be seen.

provides a much better fit to the data. Hayashi (1997) also found that Sedov model fits to the *ASCA* data of IKT 22 gave the most reliable results. We also fit, based on the high mass estimates for the NEI fits, the DEM S 32, IKT 2, HFPK 419, and IKT 16 spectra with a Sedov model.

The free parameters of the Sedov model are the normalisation ($n_e n_H R^3/d^2$), shock temperature (T_s), ionisation parameter ($I_t = n_e t_i$), elemental abundances and the column density N_H of absorbing gas. Here n_e is the pre-shock electron density, t_i is the ionisation age of the remnant, R is the SNR shock radius and d is the distance to the source. The fitting procedure for the Sedov models is the same as in the case of the NEI models. The fit results are summarised in Table 4.

From these fits, we can estimate several physical parameters for the SNRs in question. If n_e is the electron density, n_H is the hydrogen density, n_m is the total number density of protons+neutrons (including those bound up in nuclei), then, using the elemental abundances and assuming a fully ionised plasma we can calculate the number of electrons per hydrogen atom $r_e = n_e/n_H$ and the effective number of protons and neutrons (baryon mass) per hydrogen atom $r_m = n_m/n_H$. By adopting the values of the parameters mentioned above we estimate the electron density (n_e), the hydrogen density (n_H), the Sedov dynamical age (t_{dyn}), the effective ionisation age (t_i), the total emitting mass (M) and initial explosion energy (E_0) by using:

$$n_e = \sqrt{N r_e d^2/R^3},\ \mathrm{m}^{-3} \quad (1)$$

$$n_H = \sqrt{N d^2/(R^3 r_e)},\ \mathrm{m}^{-3} \quad (2)$$

$$t_{dyn} = 1.3 \times 10^{-14} R/\sqrt{T_s},\ \mathrm{yr} \quad (3)$$

$$t_i = 3.17 \times 10^{-8} I_t/n_e,\ \mathrm{yr} \quad (4)$$

$$M = 5 \times 10^{-31} m_p r_m n_H V,\ M_\odot \quad (5)$$

$$E_0 = 2.64 \times 10^{-15} T_s R^3 n_H,\ \mathrm{J}. \quad (6)$$

Here N is the normalisation (m^{-5}), m_p (kg) is the proton mass, R (m) is the shock radius, T_s (keV) is the shock temperature, I_t (m^{-3} s) is the ionisation parameter and $V(=4/3\pi R^3)$ is the total volume. We do not apply a volume filling factor to our estimates (Eqs. (1)–(6)) as it is already implicitely contained within the Sedov model. We assume that the remnants are spherically symmetric. The results are given in Table 5. The mass estimates based on the NEI fits compare well to those

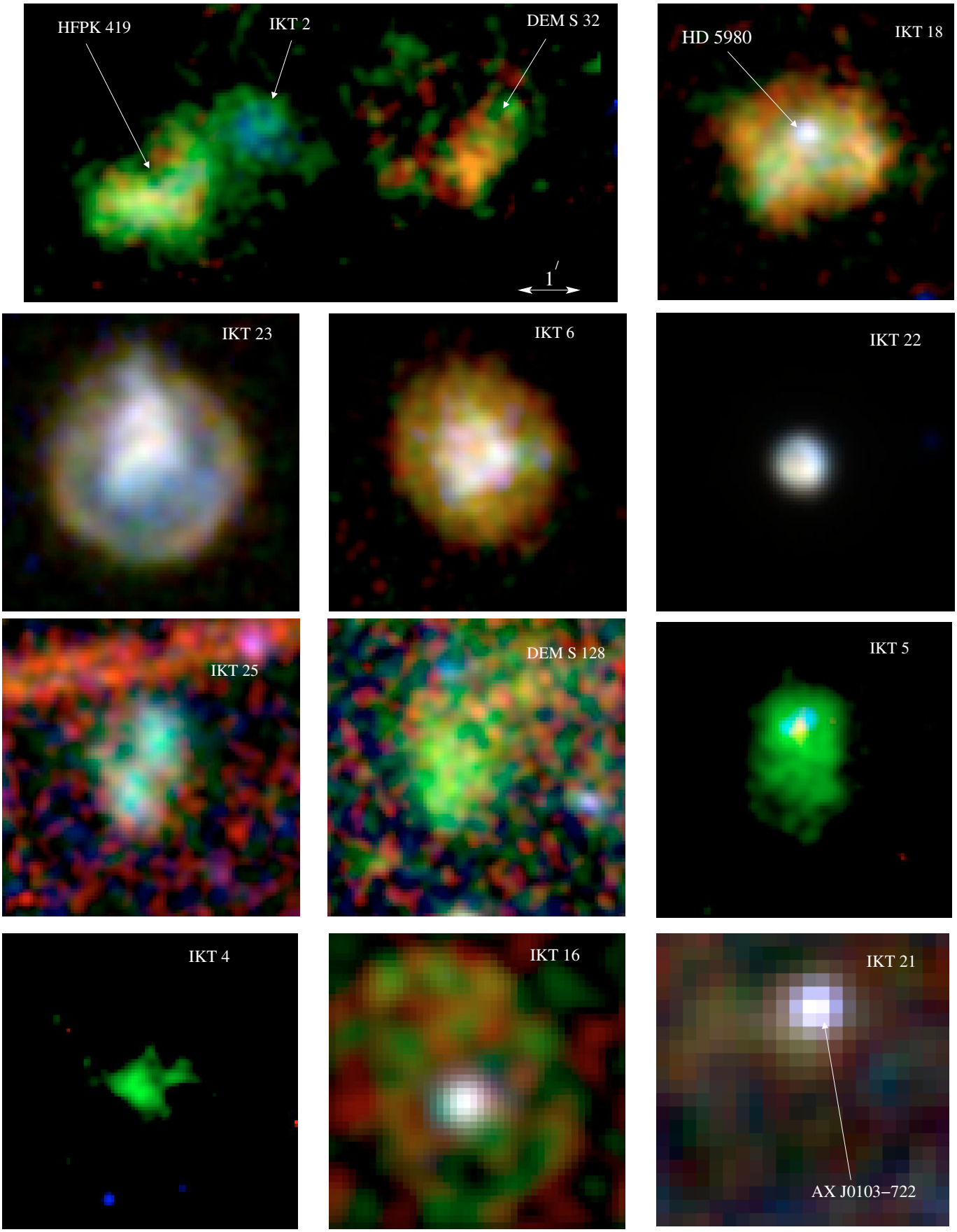

Fig. 2. Details of the remnants in our sample. Red, green and blue represents the 0.5–0.7 keV, 0.7–1.0 and 1.0–3.0 keV energy bands. All the images are on the same plate scale, as indicated in the upper left image.

Table 2. Log of the SNRs in our field.

Object*	SNR Cat.	Obs. ID	RA (J2000)	Dec (J2000)	Count rate (PN) counts/s	Point source cont. %
DEM S 32	0044-73.4	0110000101	00 46 39.1	−73 08 39	0.034 ± 0.002	–
IKT 2	0045-73.4	0110000101	00 47 12.2	−73 08 26	0.034 ± 0.002	–
HFPK 419	(0045.8-73.4)	0110000101	00 47 40.6	−73 09 30	0.087 ± 0.003	–
IKT 4	0046-73.5	0110000101	00 48 24.8	−73 19 24	0.03 ± 0.002	–
IKT 5	0047-73.5	0110000101	00 49 06.9	−73 14 05	0.124 ± 0.004	–
IKT 6	0049-73.6	0110000101	00 51 06.5	−73 21 26	0.482 ± 0.006	–
IKT 16	0056-72.5	0110000201	00 58 16.4	−72 18 05	0.088 ± 0.005	2
IKT 18	0057-72.2	0110000201	00 59 25.4	−72 10 10	0.383 ± 0.007	1
IKT 21	0101-72.4	0123110201	01 03 12.8	−72 08 59	0.120 ± 0.006	35
IKT 22	0102-72.3	0123110201	01 04 02.0	−72 01 48	18.78 ± 0.04	–
IKT 23	0103-72.6	0110000301	01 05 03.5	−72 22 56	2.40 ± 0.01	–
DEM S 128	(0103-72.4)	0123110201	01 05 23.2	−72 09 26	0.042 ± 0.005	3.5
IKT 25	0104-72.3	0123110201	01 06 14.3	−72 05 18	0.092 ± 0.006	15

* Abbreviations used
DEM S Hα catalogue of emission nebulae (Davies et al. 1976).
IKT X-ray catalogue (Inoue et al. 1983).
HFPK X-ray catalogue (Haberl et al. 2000).

obtained from the Sedov model fits. However, any deviation from symmetry (e.g. fragmentary shells) or sphericity will, of course, affect the volume estimates which in turn influences the estimates of derived parameters such as densities, explosion energy and mass. The effect of an incorrect volume estimate on the derived parameters can be estimated by applying a volume factor $f = \sqrt{V_t/V_s}$, where V_t is the true emitting volume and V_s is the estimated volume for spherical symmetry. The following corrections would then hold: (n_e, n_H, E_0)×$1/f$ and (M, t_i)×f. For example, an ellipsoidal morphology with one axis 20% larger than the radius of a sphere would give $f \sim 1.1$.

We also fit the spectra from the inner regions of IKT 6 and 23. As a model we use one NEI component to account for emission from the central region. In addition to this, we added the same plasma component and parameters as derived from the fits to the outer region, only the normalisations from these components were allowed to vary. This method accounts for any projected fore/background shell emission. The fit results supplied in Table 3, are very similar between the two remnants.

The best fit models generally provides good fits to the data, though a few discrepancies exist. Uncertainties in the modeling of the data include the calibration differences between the EPIC-pn and EPIC-MOS and incompleteness of the atomic database. For example, the most prominent residual is the underestimation of the spectra at ≈1.2 keV. This is a known problem and is probably due to missing high excitation lines of Fe XVII-XIX in the plasma code (see Brickhouse et al. 2000).

Shock waves in the shells of SNRs are thought to be collisionless because at the low densities encountered in remnants the shock front is thinner than the mean free path for collisions. The actual heating mechanism in collisionless shocks is not straightforward and needless to say, not well understood. The heating of particles at the shock-front is thought to be produced by collective processes, such as plasma waves (for a review see for instance, Draine & McKee 1993; Laming 2000). Since the heating is not collisional the plasma can be regarded as a two fluid system consisting of electrons and ions. There is no guarantee that there will be equilibration between the electron and ion temperature. We therefore investigated the effect of non-equipartion on our derived parameters, as our model fits assume equilibration between electron and ion temperatures. We fitted a sample of our brighter remnants with a Sedov model in which the electron temperature lags the shock temperature (see Borkowski et al. 2001). We initially left both the shock and electron temperature free, but both these values tracked each other. We then imposed fixed shock to electron temperature ratios of 0.5 and 0.2. We found that the derived parameters, except for the ionisation parameter and emission measure, did not differ significantly from the electron-ion temperature equilibration models. In fact, we obtained slightly better fits (in terms of reduced χ^2) with the equilibration models. This could be because most of our remnants are evolved and have already attained or are approaching electron-ion temperature equilibration.

4. Discussion

4.1. Progenitor types

4.1.1. Core-collapse candidates

IKT 6 and IKT 23 are remarkably similar remnants, both morphologically and spectrally (Figs. 3 and 4). IKT 23 has a clear shell and a centrally filled morphology. The colours in Fig. 2 indicate that the outer region is softer than the inner region. IKT 6 exhibits a similar morphology, although it is not as clearly resolved. IKT 6 is located towards the edge of the detector where the effective area and spatial resolution is lower. The other remnant in our sample with a clear shell structure is IKT 22. This remnant is quite striking since it is orders of magnitude more luminous than the other SNRs in the field.

The spectra extracted from the two regions (i.e. outer and inner) of IKT 6 and IKT 23 (see Figs. 3 and 4) are distinctly different. However, the spectra are remarkably similar between the two remnants. The spectral fitting results given in

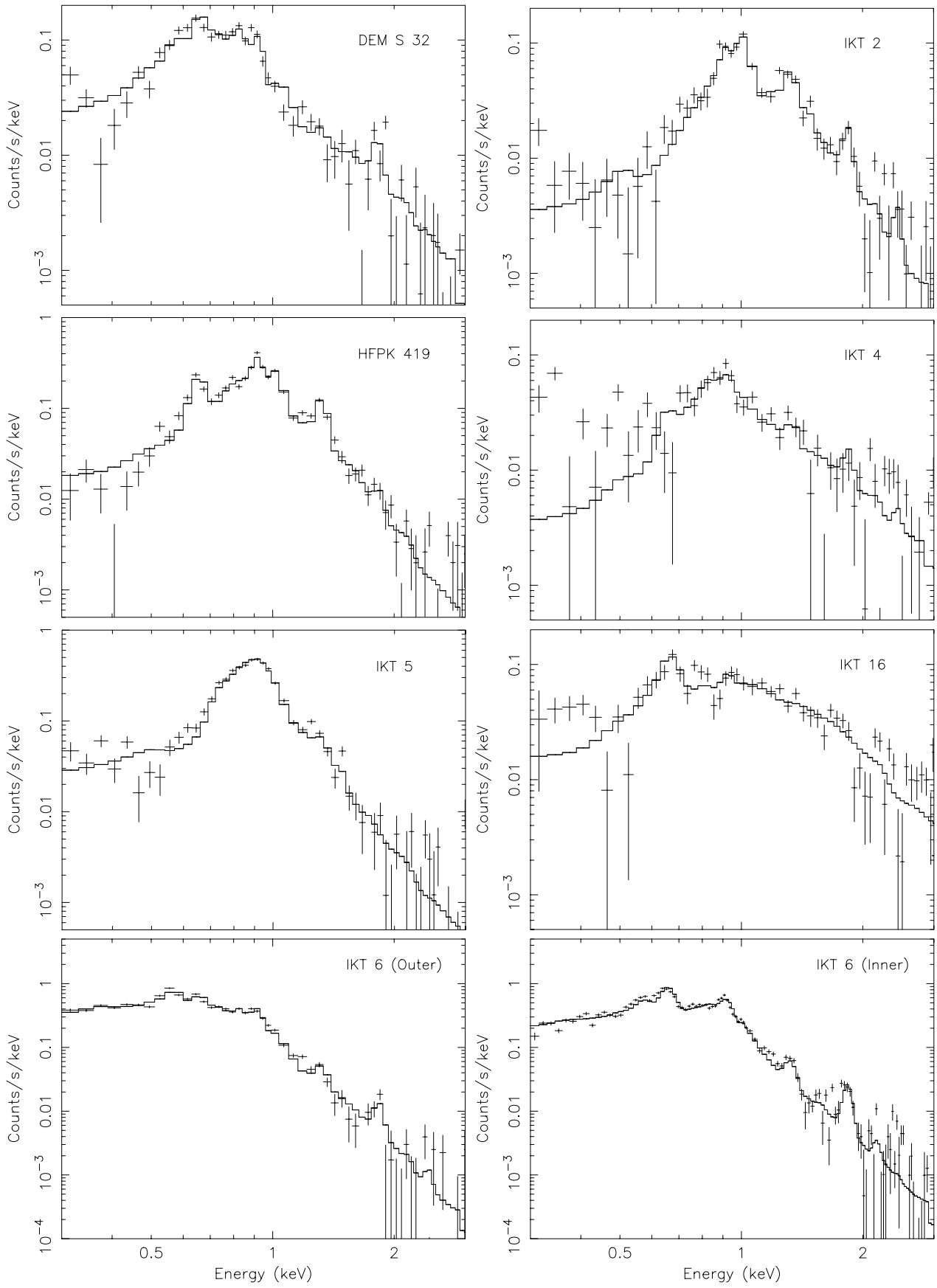

Fig. 3. Combined EPIC (i.e. EPIC-pn+EPIC-MOS) background-subtracted spectra of individual SNRs. The crosses represent the data points and error bars and the solid histogram represent the best fit models (i.e. Sedov model for all spectra appearing in Table 4, and the single temperature NEI model for the rest).

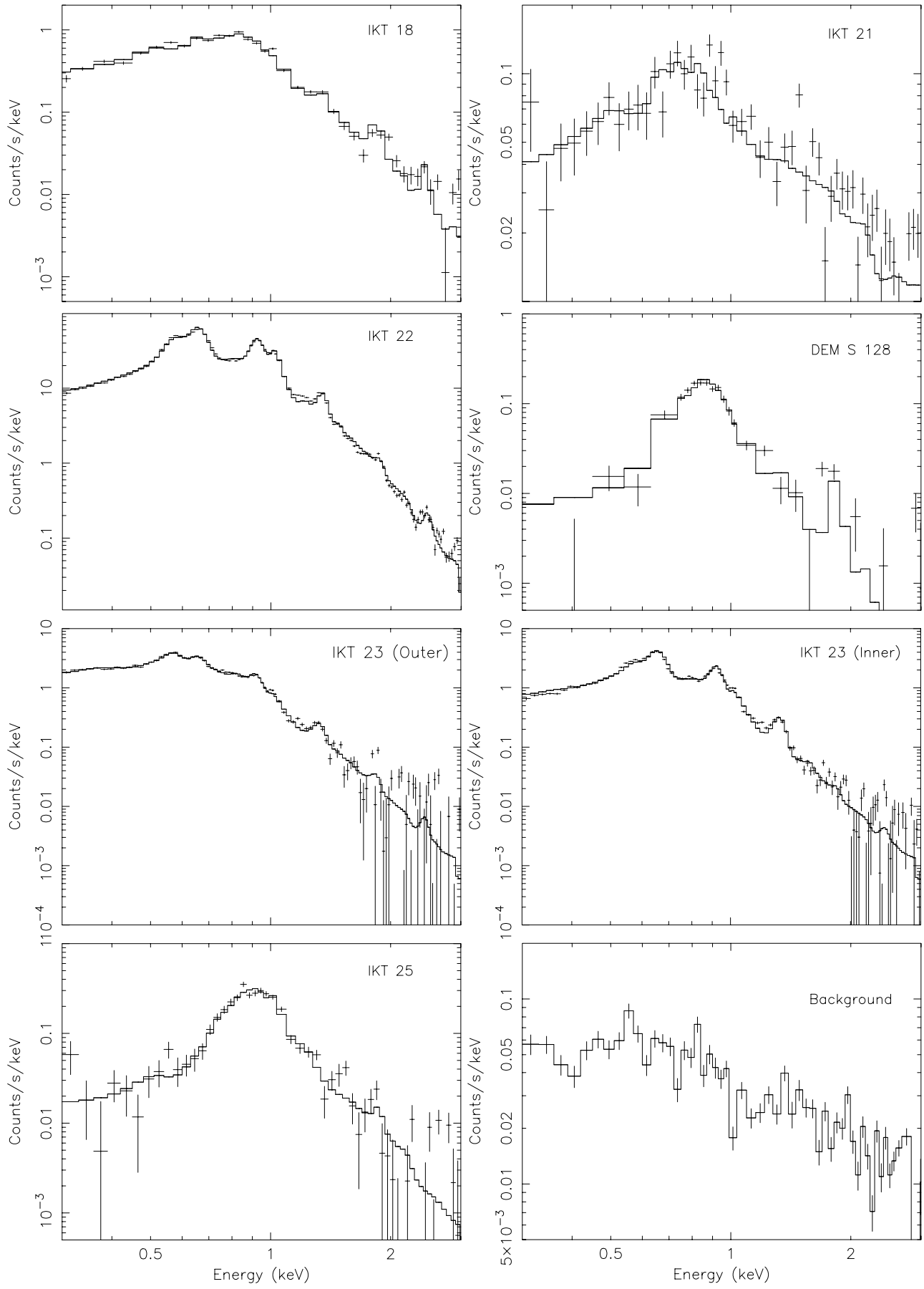

Fig. 4. Same as for Fig. 3. The lower right panel represents a typical background spectrum.

Table 3. NEI model spectral fitting results. The fit errors (1σ) are given in brackets. The abundances are all relative to their solar values (Anders & Grevese 1989).

SNR	Radius (arcsec)	$N_{\rm H}$ (10^{25} m^{-2})	$n_{\rm e}n_{\rm H}V$ (10^{64} m^{-3})	$kT_{\rm e}$ (keV)	$n_{\rm e}t$ (10^{16} m^{-3} s)	$n_{\rm e}$ (10^{6}) m^{-3}	Mass $M_{\odot}$
DEM S 32	68	2.4(0.7)	0.60(0.25)	1.51(0.48)	1.0(4.5)	0.18	39
IKT 2	33	3.9(1.5)	1.5(1.4)	0.77(0.59)	>20.0	0.84	21
HFPK 419	45	3.9(1.5)	1.21(1.1)	0.62(0.39)	>13.0	0.48	30
IKT 4	42	6.2(0.9)	0.14(0.03)	3.5(1.4)	2.1(0.2)	0.18	9
IKT 5	58	1.1(0.9)	0.47(0.23)	0.71(0.04)	>48.0	0.20	27
IKT 6	74	0.6(0.2)	5.9(0.8)	0.54(0.03)	3.5(0.4)	0.50	139
IKT 16	100	0.6(0.5)	1.9(0.4)	1.6(0.4)	0.37(0.07)	0.17	104
IKT 18	79	2.5(0.5)	9.1(3.5)	0.57(0.12)	2.7(+100)	0.56	190
IKT 21*	31	2.0(0.8)	0.48(0.31)	0.58(0.40)	4.3(+100)	0.53	11
IKT 22	24	1.1(0.1)	73.2(5.6)	0.38(0.01)	>600	9.62	93
IKT 23	99	0.4(0.1)	9.3(1.3)	0.68(0.04)	2.5(0.4)	0.41	270
DEM S 128	62	1.8(1.2)	0.17(0.12)	0.61(0.13)	>200	0.11	18
IKT 25	55	4.8(1.7)	1.2(0.5)	0.60(0.11)	38(20.0)	0.36	40
IKT6-inner	30	0.8(0.1)	0.13(0.06)	0.89(0.16)	5.4(2.1)	0.29	5
IKT23-inner	40	1.1(0.1)	0.22(0.08)	0.92(0.12)	2.8(0.5)	0.25	11

SNR	O	Ne	Mg	Si	Fe	$L_{\rm x}$(0.5–2 keV) (10^{27} W)	χ^2/d.o.f.
DEM S 32	0.20(0.06)	0.23(0.08)	<0.10)	0.29(0.21)	0.08(0.05)	19	190/151
IKT 2	<0.10	0.81(0.42)	0.72(0.35)	0.41(0.13)	0.13(0.09)	14	152/155
HFPK 419	1.2(0.9)	1.9(1.5)	1.6(1.4)	0.24(0.19)	0.39(0.34)	42	192/155
IKT 4	0.2(f)	0.2(f)	0.2(f)	0.2(f)	0.2(f)	18	205/155
IKT 5	<0.1	0.92(0.65)	0.93(0.45)	<0.1	0.91(0.35)	9.6	340/320
IKT 6	0.11(0.01)	0.24(0.03)	0.17(0.04)	0.42(0.2)	0.09(0.01)	66	610/320
IKT 16	0.2(f)	0.2(f)	0.2(f)	0.2(f)	0.2(f)	61	162/109
IKT 18	0.06(0.02)	0.09(0.04)	0.07(0.03)	0.25(0.1)	0.07(0.1)	62	333/153
IKT 21	0.20(f)	0.20(f)	0.20(f)	0.20(f)	0.20(f)	8.0	416/361
IKT 22	2.0(0.1)	2.5(0.2)	1.5(0.1)	0.65(0.09)	0.10(0.01)	150	3043/212
IKT 23	0.14(0.01)	0.28(0.02)	0.21(0.02)	<0.1	0.07(0.01)	150	1103/320
DEM S 128	<0.1	<0.1	2.6(1.1)	2.4(1.6)	2.34(1.1)	7.8	125/115
IKT 25	<0.1	3.0(1.2)	<0.1	<0.1	1.5(0.4)	45	139/156
IKT6-inner	2.0(0.6)	2.3(0.8)	1.6(0.9)	2.7(1.2)	0.87(0.31)	17	180/155
IKT23-inner	2.1(0.5)	4.7(1.2)	3.3(1.3)	0.2(f)	0.55(0.15)	37	410/320

* plus power-law component, norm. $\sim 2.2 \times 10^{43}$ phs^{-1} keV^{-1} and $\gamma \sim 0.9$.

$^{+}$f – fixed.

Tables 3 and 4 also yield similar parameters for the two remnants. Although not clearly visible in the *XMM-Newton* data (because of the lower spatial resolution), the *Chandra* data do reveal that IKT 22 has a blastwave and reverse shock structure (Hughes et al. 2000). The spectra from these two regions are also distinctly different.

The abundance derived from the fits to the outer regions of IKT 6 and IKT 23 are consistent with the SMC ISM abundances, while the inner regions reveal much higher abundance values. We propose, based on the abundance profiles, that the inner region represents reverse shock heated ejecta material while the outer region represents a blastwave moving through the ISM/CSM. The fit results also show that the inner (ejecta-rich) regions are hotter ($kT \sim 0.9$ keV) than the outer regions ($kT \sim 0.27$ keV). This is expected from models such as proposed by Truelove & McKee (2001), which predict that the blastwave in more evolved remnants eventually attains a lower velocity than the reverse shock.

The spectra extracted from the inner regions of IKT 6 and IKT 23 are also similar to the IKT 22 spectrum. All three remnants show enhanced O, Ne and Mg abundances with respect to Fe. The abundance values of these elements (w.r.t. solar) are

Table 4. Sedov model spectral fitting results. The fit errors (1σ) are given in brackets. The abundances are all relative to their solar values (Anders & Grevese 1989).

SNR	$N_{\rm H}$ (10^{25} m^{-2})	$n_{\rm e}n_{\rm H}R^3/d^2$ (10^{20} m^{-5})	$kT_{\rm e}$ (keV)	$n_{\rm e}t$ (10^{16} m^{-3} s)	$L_{\rm x}$(0.5−2 keV) (10^{27} W)
DEM S 32	1.9(0.6)	1.70(0.7)	1.29(0.46)	2.5(1.1)	16
IKT 2	5.1(1.2)	16.3(9.3)	0.39(0.05)	>220	20
HFPK 419	4.4(0.9)	12.7(5.2)	0.28(0.03)	>360	57
IKT 6-outer	0.7(0.2)	22.5(7.5)	0.27(0.05)	11.1(0.5)	39
IKT 16	5.1(0.6)	4.32(1.8)	1.76(0.65)	0.51(0.1)	39
IKT 18	1.3(0.2)	15.4(5.1)	0.51(0.06)	20.0(10.1)	39
IKT 22	0.60(0.06)	99.3(11)	0.78(0.08)	9.0(+1.7)	1.3×10^3
IKT 23-outer	0.5(0.1)	51.9(5.8)	0.26(0.03)	20.0(0.4)	85

SNR	O	Ne	Mg	Si	Fe	χ^2/d.o.f.
DEM S 32	0.28(0.15)	0.17(0.14)	0.19(0.14)	0.45(0.26)	0.23(0.1)	164/149
IKT 2	<0.08	0.89(0.39)	0.51(0.23)	0.33(0.17)	<0.1	152/149
HFPK 419	1.25(0.45)	2.19(0.74)	1.65(0.54)	0.13(0.1)	0.25(0.1)	193/150
IKT6-outer	0.13(0.03)	0.28(0.08)	0.3(0.12)	0.4(0.3)	0.15(0.04)	223/155
IKT 16	0.2(f)	0.2(f)	0.2(f)	0.2(f)	0.2(f)	199/165
IKT 18	0.14(0.07)	0.11(0.07)	0.22(0.09)	0.44(0.13)	0.17(0.03)	253/153
IKT 22	0.87(0.05)	1.99(0.10)	1.32(0.09)	0.21(0.03)	0.29(0.02)	841/211
IKT23-outer	0.17(0.02)	0.28(0.04)	0.35(0.07)	0.36(0.15)	0.11(0.02)	460/320

Table 5. Physical parameters derived from the best fit Sedov model results.

SNR	$n_{\rm e}$ (10^6 m^{-3})	$n_{\rm H}$	$t_{\rm i}$ (10^3 yrs)	$t_{\rm dyn}$ (10^3 yrs)	Mass ($M_\odot$)	E_0 (10^{44} J)
DEM S 32	0.05	0.05	15	6	43	0.9
IKT 2	0.45	0.44	>34	5.4	47	0.3
HFPK 419	0.26	0.25	>50	8.5	64	0.6
IKT 6-outer	0.21	0.17	18	14	180	0.8
IKT 16	0.05	0.04	3.5	7.5	124	3.4
IKT 18	0.13	0.11	23	11	196	1.2
IKT 22	2.03	1.68	1.4	2.7	84	0.8
IKT 23-outer	0.19	0.16	30	19	424	1.8

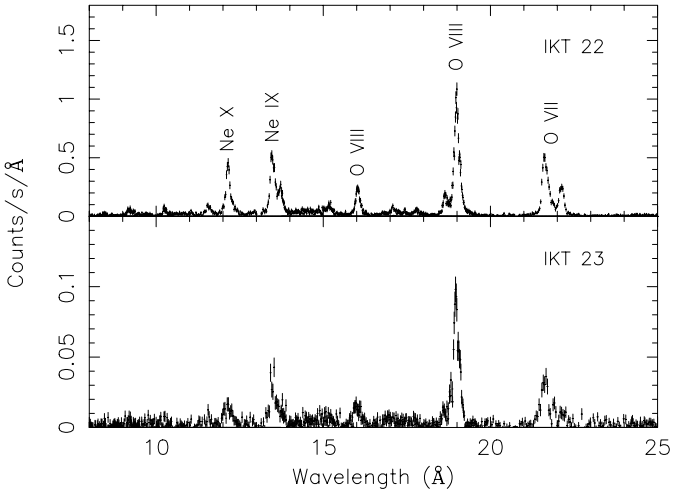

Fig. 5. RGS spectrum of IKT 22 (*top*) and IKT 23 (*bottom*). The most prominent emission lines are labeled.

Table 6. Comparison of the O, Ne and Mg complexes (error weighted mean) to the Fe abundance values for the core-collapse and type Ia candidates

SNR	(O, Ne and Mg)	Fe
Core-collapse candidates:		
IKT 22	1.14(0.04)	0.29(0.02)
IKT 23-inner	2.58(0.43)	0.55(0.15)
IKT 6-inner	2.00(0.42)	0.87(0.31)
IKT 2	0.59(0.19)	<0.1
HFPK 419	1.55(0.31)	0.25(0.11)
IKT 16	0.2(f)	0.2(f)
Type Ia candidates:		
IKT 5	0.28(0.16)	0.91(0.35)
DEM S 128	0.14(0.10)	2.34(1.10)
IKT 25	0.14(0.10)	1.5(0.4)

also an order of magnitude larger than their SMC ISM values. We also obtained RGS spectra of IKT 22 and IKT 23. The spectra were extracted from the entire remnants. The high-resolution RGS spectra of IKT 22 and IKT 23, displayed in Fig. 5, again bear striking similarities and reveal prominent emission lines of O and Ne species. The most obvious difference between the two spectra is in the count rate. The flux in the emission lines of IKT 22 are an order of magnitude larger than compared to IKT 23. Much of this flux difference can be attributed to the differences in abundance values. This is because the RGS (and EPIC) spectrum of IKT 22 is dominated by emission from ejecta-rich material, while the IKT 23 spectrum is dominated by emission from the swept-up ISM material, which has an average abundance of ∼0.2 solar. Fits to the EPIC data extracted from the entire remnant also show that the

abundances for IKT 22 are an order of magnitude larger than compared to IKT 23. A more detailed RGS analysis of IKT 22 is provided by Rasmussen et al. (2001).

The similarities between IKT 6, IKT 22 and IKT 23 suggests that these three remnants have common progenitors. IKT 22 is a well studied remnant that has been classified as being the result of a core-collapse SN. IKT 6 and IKT 23 should thus also be the remnants of core-collapse SNe. Both the derived abundances and masses for the inner regions of IKT 6 and IKT 23 are consistent with this interpretation. These remnants represent very different stages of SNR evolution. IKT 22 is a ∼2000 yr old remnant (Blair et al. 1989) while IKT 6 and IKT 23 are much more evolved (14 000–20 000 yr). We propose that IKT 6 and IKT 23 are evolved versions of IKT 22 and studying these remnants in more detail presents a unique opportunity to probe the evolution of oxygen-rich remnants in the SMC. It is also interesting to note that the ejecta are still visible in remnants as evolved as IKT 6 and IKT 23.

IKT 2 and HFPK 419 are located in the large emission nebulae N19. These remnants have rather irregular and complicated X-ray morphologies. For example, it is not clear whether IKT 2 and HFPK 419 are indeed two separate remnants or part of a larger SNR. However, the spectra from these remnants are rather different, which indicate that they might actually be two separate objects. IKT 2 and HFPK 419 both show high metal abundances, which indicate that much of the X-ray emission is from ejecta enriched material. Their abundance profiles show a similar pattern in that the Ne and Mg abundances are higher than Fe (see Table 4). While the Ne and Mg abundances are enhanced above the SMC mean by only $2-3\sigma$, the error weighted mean O, Ne and Mg abundances, as supplied in Table 6, are enhance at the $3-5\sigma$ level. Furthermore, the Si and Fe abundances are lower and in line with their SMC values. The enhanced Ne and Mg abundances, as compared to the Si and Fe values, indicate a core-collapse origin (e.g. Nomoto et al. 1997; Woosley & Weaver 1995). We thus suggest, based on their abundance profiles, that these remnants are the results of core-collapse SNe. This is also in agreement with their surroundings which suggest recent, at least modest, starburst activity (Dickel et al. 2001). Yokogawa et al. (2002) analysed *ASCA* and *ROSAT* data of IKT 2 and also find enhanced abundances, even though their age estimate is rather large. They suggest that IKT 2 is the result of a core collapse SN with a progenitor mass of $\lesssim 20\ M_{\odot}$.

IKT 16 is one of the weaker X-ray sources in our sample. The X-ray morphology appears consistent with the radio and Hα classification of it being a shell like SNR (Mathewson et al. 1984). A harder emission spot can be seen in the centre of the X-ray image. This emission region was excluded spectral extraction region. We also attempted to extract a separate spectrum from this region, but the data is of insufficient quality to speculate on the X-ray nature of this region. A longer exposure observation is needed to investigate whether this source is thermal or non-thermal in nature.

Also interesting is the high explosion energy ($\sim 3.3 \times 10^{44}$ W) and low ionisation age ($t_{\rm i} \sim 3\,500$ yr) associated with IKT 16. The fit parameters are not very well constrained due to the low count rate so the discrepancies might originate from statistical limitations. However, in their analysis of the LMC remnants, Hughes et al. (1998) found a connection between low ionisation age (as compared to the dynamical age) and high explosion energy. They explain this connection as SNRs which exploded within pre-existing low-density cavities in the ISM. The remnant expands rapidly to the cavity wall, where it then encounters denser gas and begins to emit X-rays. This results in a lower dynamical age and explosion energy than that inferred from the Sedov model. A similar scenario could thus be applicable to IKT 16. If this is the case, then IKT 16 would be the result of the core-collapse of a massive star whose stellar wind has caused a low density circumstellar cavity.

4.1.2. Type Ia candidates

The images in Fig. 2 show that IKT 5, DEM S 128 and IKT 25 have similar diffuse X-ray morphologies with no clear shell like structure. The emission peaks in the 0.7–1.0 keV band. This indicates that the flux of these sources are dominated by emission from Fe–L transitions. The X-ray sizes of IKT 5, DEM S 128 and IKT 25 are much smaller than their optical or radio diameters (see Mathewson et al. 1983; Mathewson et al. 1984; Filipovic et al. 2000). The large optical diameters imply that they are evolved remnants. Mathewson et al. (1984) also attribute the high S II emission detected in IKT 5 and IKT 25 to the onset of radiative cooling due to the evolved nature of these remnants. In this scenario IKT 5, DEM S 128 and IKT 25 would have evolved to such a degree that the shells have eventually become too faint or too cool to be seen in X-rays and we only see the hotter Fe-rich ejecta remains. The morphologies and temperature structure of IKT 6 and IKT 23 also add credence to such a scenario.

We fitted the spectra of these three remnants with NEI models. Hughes & Smith (1994) reported a point source, possibly a Be-binary system, with a power law spectrum in the field of IKT 25. We thus added a power-law component to the NEI model of IKT 25. We fixed the photon index of the powerlaw to 1.5 and flux to 1×10^{-16} W m^{-2} (Hughes & Smith 1994), since we could not constrain any power-law parameters in out data. The best fit parameters are given in Table 3. These fits also show enhanced Fe abundances. Although the spectra of IKT5, DEM S 128 and IKT 25 were well fitted with an NEI model with free abundances, we could not constrain the abundances very well due to the limited statistics. What is obvious, though, is that the Fe abundance values were consistently, and at least 3σ, above the SMC mean metallicity. We also tried to fix the abundances, except for Fe, to the SMC mean, but here it is also clear that we need an enhanced Fe abundance. It is clear from Table 6 that the Fe abundance is enhanced with respect to the mean O, Ne and Mg abundance values. It has been argued (e.g., Nishiuchi et al. 2001; Hughes et al. 1995) that the excess of emission around 1 keV, interpreted as an overabundance of Fe, may suggest that the progenitor of the SNR origin was a type Ia SN. The apparent excess emission around ∼0.9 keV and the high Fe abundance in these remnants suggests that these remnants are the result of type Ia supernovae. A possible interpretation is that these remnants are much more evolved versions of SNR DEM L 71 in the LMC

(Hughes et al. 2003; van der Heyden et al. 2003). Here we see a bright ISM dominated shell with fainter Fe-rich ejecta material in the centre. However, higher spectral resolution is required to investigate the elemental abundance ratios of these remnants in more detail. It should also be noted that an association between IKT 25 and the Be-binary system would imply that this SNR would be the remnant of a massive star rather than a type Ia SN.

4.1.3. The cases of IKT 18, DEM S 32, IKT 21 and IKT 4

IKT 18 has a rectangular shape. The emission is diffuse with no obvious limb brightening. The *Chandra* data (Nazé et al. 2002) do reveal a few bright or dark arcs, but apart from these, the brightness is rather uniform. The luminous blue variable (LBV) HD 5980 can also be seen in the centre of IKT 18. The spatial coincidence of IKT 18 with the peculiar binary system HD 5980 suggests an association with this system. The possible association was recently investigated by Nazé et al. (2002). They drew attention to similarities between IKT 18 and the Carina nebula. However, they concluded that based on the non-thermal radio emission (Ye et al. 1991) and a high velocity expansion (Chu & Kennicutt 1988), IKT 18 should be regarded as a SNR with HD 5980 located behind the remnant.

The results of our NEI model fits differ from those obtained by Nazé et al. (2002) (Mekal model fits to the *Chandra* data) and Yokogawa et al. (2002) (NEI model fits to the *ASCA* data) in that our column density is a factor of 2 higher and our abundances are generally lower. However, Yokogawa et al. (2002) fixed their abundance values to 0.2 times solar while the model used by Nazé et al. (2002) only gives a mean metallicity. It should be noted that the results obtained from fits to the *XMM-Newton*, *Chandra* and *ASCA* data set are generally consistent within the errors. All three spectral analyses give a total X-ray emitting mass estimate of 100–200 $M_{\odot}$, which indicate that this remnant is in the Sedov evolutionary stage. We thus proceeded to fit our data with a Sedov model. This model gave abundances profiles which are very much in line with the SMC ISM abundances of Russel & Dopita (1992). The low SMC-like abundances and high mass (196 $M_{\odot}$) and age estimate (11 000 yr) derived from our fits are also consistent with the picture of an evolved SNR which has swept-up ISM material. While the low abundances do not allow for a progenitor typing, Yokogawa et al. (2002) argue that the location in a giant H II region favours a type II origin. More *XMM-Newton* data will be available in the near future, which will allow for a more detailed assessment of the nature of this object.

DEM S 32 is another remnant, as is IKT 2 and HFPK 419, in the vicinity of N19. It has a shell-like structure with enhanced emission towards the southwestern limb. The abundance yields from DEM S 32 are lower than for IKT 2 and HFPK 419 and no clear distinction in progenitor type can be infered from these yields. The environment (N19), however, might suggest that DEM S 32 has a massive star progenitor and is thus possibly the result of a core-collapse SN explosion.

There is no clear X-ray emission associated with the optical emission from IKT 21. The X-ray emission from the vicinity of the optical remnant is dominated by the Be-pulsar binary system AX J0103-722 (Hughes & Smith 1994; Israel et al. 2000). We extracted our spectrum from the region containing the optical emission, which includes the pulsar system. Although not visible in Fig. 4, the spectrum clearly extends above 3 keV. Our model for IKT 21 thus consists of a NEI component for thermal emission from the SNR and a power-law component to account for the pulsar emission. The power-law component normalisation and photon index were initially fixed to values obtained from Hughes & Smith (1994) and were subsequently allowed to vary. The best fit model gives a power-law component normalisation of $\sim 2.2 \times 10^{43}$ ph s^{-1} keV^{-1}, a photon index of ~0.9 and a luminosity of $\sim 5.5 \times 10^{27}$ W (0.5–2.0 keV band). Our results for the thermal emission indicate a temperature of $kT_{\rm e} \sim 0.58 \pm 0.40$ and a luminosity of $\sim 8 \times 10^{27}$ W (0.5–2.0 keV band). These results compare well with estimates obtained by Hughes & Smith (1994). It is not clear whether the pulsar AX J0103-722 is associated with the SNR as it is not near the centre of the remnant. An association would mean that IKT 21 would be the remnant of a massive-star SN (Hughes & Smith 1994).

IKT 4 has a very similar morphology to IKT 5, DEM S 128 and IKT 25. Its X-ray emission, which peaks in the Fe-*L* band, lies inside its optical emission. The spectrum is too weak to constrain the abundance, so we cannot speculate on its progenitor based on the spectrum. However, the morphology does argue for a type Ia SN origin.

4.2. SMC abundances

The abundance values for the swept-up matter dominated SNRs (Table 4) show some spread among the remnants and also between different elemental species. The general trend is that the larger remnants have lower abundance values while the smaller ones have larger values. The interpretation is that the older remnants have swept-up so much ISM material that the abundances are approaching the ISM values. The abundance yields from the older remnants with larger swept-up masses could thus be used to probe the ISM abundance distribution.

We use the abundances derived from the spectral fits to IKT 6 (outer region), IKT 18 and IKT 23 (outer region) to determine the gas-phase abundances of the SMC. These remnants are selected because of their high (swept-up) masses. We average, for each elemental species, the fitted abundances from the three remnants. In Fig. 6 we plot the error weighted average abundances versus elemental species. The uncertainties represent the rms-scatter among the remnants. The derived abundances are also compared to the average SMC abundance values presented by Russel & Dopita (1992). The work of Russel & Dopita (1992) is based on the spectral analysis of F supergiants for heavier elements ($Z > 12$) and H II regions and SNRs for lower Z elements. However, they only have 1 SMC SNR in their studies. Our average abundance values for the low-Z elements appear slightly higher than those obtained by Russel & Dopita (1992), but are in good agreement within the uncertainties.

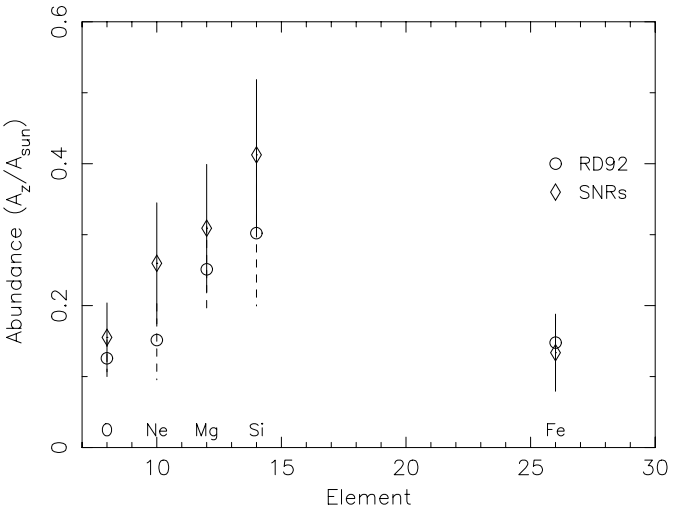

Fig. 6. Average SMC abundances. The average abundance values obtained from fits to IKT 6 IKT 18 and IKT 23 are represented by diamonds. Results from Russel & Dopita (1992) are indicated with circles.

4.3. Physical parameters

The ionisation ages given in Table 5 are generally consistent with the dynamical age within a factor 2, the exceptions being IKT 2 and HFPK 149. The factor of 2 difference can be easily be attributed to inaccurate volume estimates, which could be due to any deviation from the assumed symmetry or sphericity of the SNRs, as described in a previous section. This would afect the electron density and thus reduce the ionisation age estimates. The possibility of fragmentary shells or clumping means that the initial explosion energy E_0 and mass estimates should be regarded as lower and upper bounds respectively.

In the case of IKT 2 and HFPK 149 the plasma has reached ionisation equilibrium. In this regime the ionisation parameter becomes insensitive as an age indicator since the spectrum changes very slowly with increasing ionisation parameter.

The mean SMC ISM hydrogen density derived from the Sedov model fits is $\sim 0.32 \times 10^6$ m^{-3}. This is nearly an order of magnitude lower than the mean density of $\sim 1.8 \times 10^6$ m^{-3} derived from Sedov fits to a sample of LMC remnants by Hughes et al. (1998). The lower SMC abundance and densities easily explains the lower SNR luminosities compared to their LMC counterparts, as the X-ray emission scales with the densities. The lower abundances and densities also have implications for the dynamical evolution of SNRs in the SMC. Cox (1972) predicts that the onset of radiative cooling occurs at a time $t_{\rm cool} = 2.5 \times 10^{-2}\ E_{44}^{2/11} L^{-5/11}\ n_{\rm H}^{-7/11}$ yr where E_{44} is the explosion energy in 10^{44} J, L is the cooling coefficient in W m^3 and $n_{\rm H}$ is in m^{-3}. The radiative cooling will be governed by L and the hydrogen density, since the explosion energies derived from the SMC and LMC samples are similar. L is a strong function of elemental abundance. The SMC/LMC ratio of this coefficient is $\approx$0.6, assuming average metallicity of 0.2 and 0.35 solar for the SMC and LMC respectively. The lower hydrogen density and metallicity means that the SMC remnants take $\sim$4 times longer to reach the radiative cooling stage, compared to the LMC remnants. The SMC remnants should thus be radiating X-rays for a longer time than in the LMC. This point is illustrated by the fact that the oldest remnant in our sample is $\sim$20 000 yr while the oldest remnant in the LMC sample analysed by Hughes et al. (1998) is 10 000 yr.

4.4. Comments on SMC SN rates

A number of conflicting SMC SN rate estimates have been made. For example, Mathewson et al. (1983) gave a birth rate of one SNR per 800 yr, while Filipovic et al. (1998) gives a birth-rate of one SNR per 350 yr. Both these estimates are higher than a rate of one in every 1100–2500 yr invoked by van den Berg & Tammann (1991), which is derived from the star formation rate inferred from the total Hα luminosity of the SMC.

If we follow the arguments from the previous section (Sect. 4.3) then we estimate that the onset of the radiative cooling stage commences at $\sim$30 000 yr. Now if we consider that 16 X-ray emitting SNRs have been detected, to date, then the SN rate in the SMC should be closer to one per $\sim$1800 yr. This rate is in line with the rate inferred from van den Berg & Tammann (1991). The derived rate is also consistent with our age estimate ($\sim$2700 yr) of the youngest SMC SNR (viz. IKT 22).

Acknowledgements. We thank Jacco Vink for the use of and help with his image processing software and for valuable discussions. The results presented are based on observations obtained with *XMM-Newton*, an ESA science mission with instruments and contributions directly funded by ESA Member States and the USA (NASA). SRON is supported financially by NWO, the Netherlands Organisation for Scientific Research.

References

Anders, E., & Grevesse, N. 1989, Geochim. Cosmochim. Acta, 53, 197
van den Berg, S., & Tammann, G. 1991, ARA&A, 29, 363
Blair, W. P., Raymond, J. C., Danziger, J., & Matteucci, F. 1989, ApJ, 338, 812
Borkowski, K. J., William, J. L., & Reynolds, S. P. 2001, ApJ, 548, 820
Brickhouse, N. S., Dupree, A. K., Edgar, R. J., et al. 2000, ApJ, 530, 387
Cappellaro, E., Evans, R., & Turrato, M. 1999, A&A, 351, 459
Chu, Y.-H, & Kennicutt, R.C. 1988, AJ, 95, 1111
Cox, D. P. 1972, ApJ, 178, 159
Davies, R. D., Elliot, K. H., & Meaburn, J. 1976, Roy. Astron. Soc. Mem., 81, 89
Dickel, J. R., Williams, R. M., Carter, L. M., et al. 2001, AJ, 122, 849
Draine, B. T., & McKee, C. F. 1993, ARA&A, 31, 373
Filipovic, M. D., Pietsch, W., Haynes, R. F., et al. 1998, A&ASS, 127, 119
Filipovic, M. D., Haberl, F., Pietsch, W., & Morgan, D. H. 2000, A&A, 353, 129
Haberl, F., Filipovic, M. D., Pietsch, W., & Kahabka, P. 2000, A&ASS, 142, 41
Hayashi, I. 1997, Ph.D. Thesis, Graduate School of Science, Kyoto University
den Herder, J. W., Brinkman, A. C., Kahn, S. M., et al. 2001, A&A, 365, L7

van der Heyden, K. J., Behar, E., Vink, J., et al. 2002, A&A, 392, 955
van der Heyden, K. J., Bleeker, J. A. M, Kaastra, J., & Vink, J. 2003, A&A, 406, 141
Hughes, J. P., & Smith, R. C. 1994, AJ, 107, 1363
Hughes, J. P., Hayashi, I., Helfand, D. J., et al. 1995, ApJ, 444, L81
Hughes, J. P., Hayashi, I., & Koyama, K. 1998, ApJ, 505, 732
Hughes, J. P., Rakowski, C. E., & Decourchelle, A., 2000, ApJ, 543, L61
Hughes, J. P., Ghavamian P., Rakowski C. E., & Slane, P. 2003, ApJ, 582, L95
Inoue, H., Koyama, K., & Tanaka, Y. 1983, in Supernova Remnants and Their X-ray Emission, ed. P. Gorenstein & J. Danziger (Dordrecht: Reidel), IAU Symp., 101, 535
Israel, G. L., Campana, S., Covino, S., et al. 2000, ApJ, 531, L131
Kaastra, J. S., Mewe, R., & Nieuwenhuijzen, H. 1996, in UV and X-ray Spectroscopy of Astrophysical and Laboratory Plasmas, ed. K. Yamashita, & T. Watanabe (Tokyo: Univ. Ac. Press), 411
Laming, J. M. 2000, ApJS, 127, 409
Massey, P., Lang, C. C., DeGioia-Eastwood, K., & Garmany, C. D. 1995, ApJ, 438, 188
Mathewson, D. S., Ford, V. L., Dopita, M. A., et al. 1983, ApJS, 51, 345
Mathewson, D. S., Ford, V. L., Dopita, M. A., et al. 1984, ApJS, 551, 189
Mewe, R., Kaastra, J. S., & Liedahl, D. A. 1995, Legacy 6, 16
Migliazzo, J., Canizares, C. D., Flanagan, K., Pannuti, T., & Fredericks, A. 2002, APS Meet., 47, N17039
Nazé, Y., Hartwell, J. M., Stevens, I. R., et al. 2002, ApJ, 580, 225
Nishiuchi, M. 2001, Ph.D. Thesis, Kyoto University
Nishiuchi, M., Yokogawa, J., Koyama, K., & Hughes J.P. 2001, PASJ, 53, 99
Nomoto, K., Iwamoto, K., Nakasato N., et al. 1997, Nucl. Phys. A, 621, 467
Rasmussen, A., Behar, E., Kahn, S. M., et al. 2001, A&A, 365, L231
Russel, S. C., & Dopita, M. A. 1992, ApJ, 384, 509
Sedov, L.I. 1959, Similarity and Dimensionless Methods in Mechanics (New York: Academic)
Strüder, L., Briel, U. G., Dennerl, K., et al. 2001, 365, L18
Truelove, J. K., & McKee, C. F. 1999, ApJS, 120, 299
Turner, M. J. L., Abbey, A., Arnaud, M., et al. 2001, 365, L27
Wang, Q., & Wu, X. 1992, ApJS, 78, 391
Westerland, B. E. 1990, A&ARv, 2, 29
Woosley, S. E., & Weaver, T.A. 1995, ApJS, 101, 181
Ye, T., Turtle, A. J., & Kennicutt, R. C. 1991, MNRAS, 249, 722
Yokogawa, J., Imanishi, K., Koyama, K., & Nishiuchi, M., & Mizuno, N. 2002, PASJ, 54, 53